ELSEVIER

Cement & Concrete Composites 26 (2004) 861–871

Cement & Concrete Composites

www.elsevier.com/locate/cemconcomp

Simulation of shrinkage induced cracking in cement composite overlays

John E. Bolander Jr. *, Stefano Berton

Department of Civil and Environmental Engineering, University of California, One Shields Ave., Davis, CA 95616-5294, USA

Received 9 December 2002; accepted 23 April 2003

Abstract

A random lattice is used to model moisture transport in cement-based composites. Model geometry, and the scaling of the elemental diffusivity terms, are based on a Voronoi discretization of the material domain. Steady-state and transient potential flow problems are simulated, and compared with theory, to demonstrate model accuracy and objectivity with respect to lattice random geometry. A novel routine is described for computing moisture flux values at the random lattice sites.

Stress production, and potential shrinkage crack development, are driven by the associated drying processes. The random lattice modeling of moisture movement is coupled with rigid-body-spring networks (RBSN), which account for elasticity, creep, and fracture properties of the material. The RBSN is based on the same Voronoi discretization of the material as used to model moisture movement. Relative humidity contours, stress contours, and crack plots are produced for a cement composite overlay restrained by a mature concrete substrate. That example is based on a set of simulation results reported in the literature.

Keywords: Moisture transport; Shrinkage; Fracture; Durability; Lattice model

1. Introduction

Protective and repair/retrofit overlay systems for structural concrete are designed from an empirical basis, despite their importance with respect to safety, serviceability and economy of the structural system. There is a need for understanding and predicting the overlay system response to mechanical and environmental loading, but advances in this area have been limited by the complexity of the problem. The overlay and substrate materials generally have quite different mechanical and hygral properties [1,2]. These materials, and their interface, also tend to be fracture sensitive and an adequate description of crack propagation in these components requires the use of nonlinear fracture mechanics [3,4]. Model-based simulation is one promising means for studying the durability aspects of such overlay systems, where the interactions between the aging, drying overlay and the more mature substrate need to be analyzed in the time domain. Computer-based tools have been developed to interactively study the influence of the various parameters that affect stress production and potential cracking in bonded concrete overlays [5]. The durability mechanics of cement composites and concrete life-cycle simulation are important areas of research that are supported by model-based simulation [6,7].

Recently, various physical phenomena have been studied using lattice models, which are composed of simple spring-like elements connected on dense nodal arrays that are either regularly or randomly distributed [8]. One active area of research is the application of lattice models to simulating fracture and transport mechanisms in cement-based composites [9–11]. In our work, a random lattice is used to model moisture transport caused by drying of the cement composite. Rigid-body-spring networks [12,13], utilizing the same lattice sites and topology, represent the corresponding shrinkage and potential cracking associated with such drying. Preliminary results are given for cracking induced by drying of an overlay on a mature concrete substrate, as affected by the elasticity, hygral, and fracture parameters of the composite system. While the ultimate goal is the explicit modeling of heterogeneity

* Corresponding author. Fax: +1-530-752-7872.
E-mail address: jebolander@ucdavis.edu (J.E. Bolander Jr.).

0958-9465/$ - see front matter © 2003 Elsevier Ltd. All rights reserved.
doi:10.1016/j.cemconcomp.2003.04.002

within the simulations, this preliminary work focusses on some of the basic properties required for effectively conducting such simulations with random lattice models.

2. Domain discretization

The transport and elasticity properties of the material are discretized using Voronoi diagrams on a semi-random set of points [14]. The Voronoi cell associated with point i is the set of points closer to point i than all other points in the domain (Fig. 1a). The Voronoi partitioning of the material domain is robust and facilitates a high degree of pre-processing automation. Advantages of this approach include the abilities to:

- explicitly model material structure, such as the boundaries between two phases (which generally do not run along the grid lines produced by a regular triangular or square lattice). This can be done by strategically placing semi-regularly spaced points prior to random filling of the domain (Fig. 1b); and
- grade average cell size, which can be advantageous for reducing computational expense.

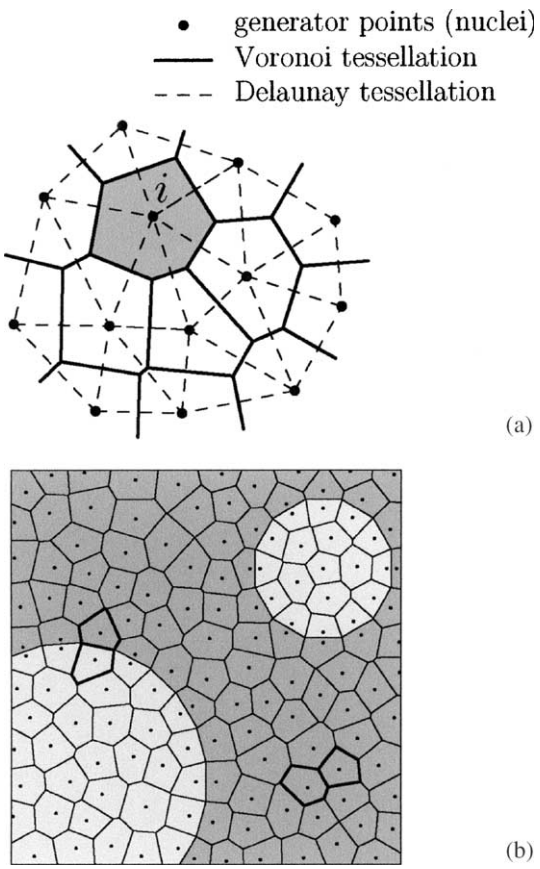

Fig. 1. (a) Dual tessellations of a two-dimensional set of points and (b) Voronoi diagram partitioning of a multi-phase material.

3. Diffusion analysis

Nonstationary potential flow problems are governed by

$$\frac{\partial u}{\partial t} = \operatorname{div}(D \operatorname{grad} u) + \gamma \tag{1}$$

for all points in the domain, Ω [15]. Here, u is the potential (e.g. relative humidity), D is diffusivity, γ accounts for internal source and sinks, and t represents time. The required boundary conditions are indicated in the examples that follow.

The potential flow problem is modeled using a random lattice, whose geometry is defined by a Voronoi diagram (or, equivalently, the Delaunay tessellation of the same set of generator points). Lineal conduit elements connect the lattice sites as shown in Fig. 2; the cross-section area of a given conduit is equal to the area of the corresponding Voronoi facet.

If potential does not vary with time, Eq. (1) simplifies to a boundary value problem governed by

$$\operatorname{div}(D \operatorname{grad} u) + \gamma = 0 \quad \text{in } \Omega \tag{2}$$

subject to

$$u = f(\mathbf{x}) \text{for } \mathbf{x} \quad \text{on } \Gamma_1 \tag{3}$$

$$q = -D\frac{\partial u}{\partial n} \text{for } \mathbf{x} \quad \text{on } \Gamma_2 \tag{4}$$

where q is outward flux normal to the boundary (i.e. in direction n) [15]; Γ_1 and Γ_2 are the boundary segments with prescribed potential and normal flux, respectively. The semi-discrete form of Eq. (2) is

$$\mathbf{K}_e\mathbf{u}_e = \mathbf{M}_e\gamma_e - \mathbf{q}_e \tag{5}$$

which involves the following elemental diffusivity and capacity matrices:

$$\mathbf{K}_e = \frac{D_e A_e}{h_e}\begin{bmatrix} 1 & -1 \\ -1 & 1 \end{bmatrix}, \qquad \mathbf{M}_e = \frac{h_e A_e}{6d}\begin{bmatrix} 2 & 1 \\ 1 & 2 \end{bmatrix} \tag{6}$$

Here, A_e is taken as the area of the Voronoi facet between the contiguous nuclei i and j. The diffusivity and

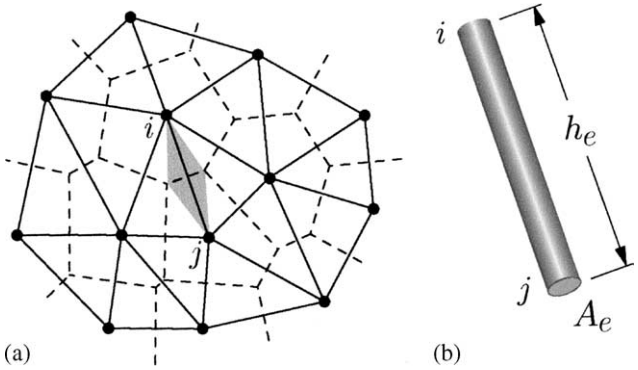

Fig. 2. Discretization for 2-D diffusion analysis: (a) conduit element ij within network, and (b) conduit element ij.

capacity matrices are the same as those of standard two-node finite elements [15], except for the capacity matrix is modified by the term A_e/d, where $d = 1.0$, 2.0, and 3.0 for 1-d, 2-d, and 3-d networks, respectively. With this extra term, the lattice element assembly is equivalent (in some situations) to a recently developed Voronoi cell finite difference approach for the diffusion operator on unstructured grids [16].

3.1. Nodal flux calculation

At any stage in the solution, the flow Q_i in the conduit element i is known from the potential difference of its nodes and the local diffusivity relations given in Eq. (6). The effects of material features within the cement composite, such as inclusions, interfaces, and defects, are lumped into the macroscopic diffusivity coefficient, D. The irregular geometry of the conduit network serves only to discretize the domain, so that the flow in the individual conduit elements has little practical meaning. However, the elemental flow values can be used to determine local measures of flux at a network node (i.e. Voronoi cell nucleus), using a method that is analogous to one developed for stress retrieval at the nodes of rigid-body-spring networks [13,17]. For the two dimensional case shown in Fig. 3, the determination of nodal flux involves:

- sectioning the associated Voronoi cell through its nucleus with a cut plane that has inclination angle ψ.
- calculating the weighting factor R_i associated with flow through each facet i of the cell. There are three possible cases for a given facet i:
  1. $R_i = 1$ when both facet vertices are located on the positive (i.e. shaded) side of the cut plane;
  2. $R_i = 0$ when both facet vertices are located on the negative side of the cut plane;
  3. $0 < R_i = a_i/b_i < 1$ when facet vertices appear on both sides of the cut plane. Here, b_i is the length of facet i and a_i is the length of the segment on the positive side of the cut plane.
- computing the net flow Q_ψ through the cut face by summing the weighted flow values for each face:

$$Q_\psi = \sum_i^n R_i Q_i \tag{7}$$

where n is the number of facets of the Voronoi cell (or, equivalently, the number of conduit elements framing into the node).

- determining the flux by dividing the net flow through the cut face by the area of the cut face, A_ψ:

$$q_\psi = Q_\psi / A_\psi \tag{8}$$

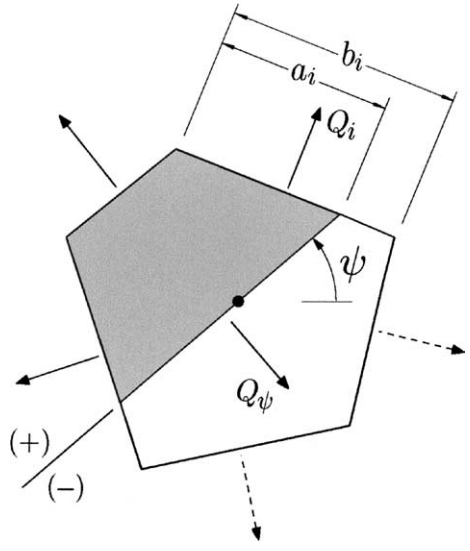

Fig. 3. Flux calculations local to Voronoi cell nucleus.

This series of calculations is repeated for increments in ψ, ranging from $\psi = 0$ to π. The maximum q_ψ (over all cut plane inclinations ψ) at each node can be used to produce flow rate contours, some of which are presented in the following section.

3.2. Steady state flow around a cylindrical inclusion

Toward the long-term goal of modeling material structure and its effect on moisture flow in concrete, the model is verified for steady-state potential flow local to a cylindrical inclusion. The computational mesh and boundary conditions are shown in Fig. 4. With no loss of generality, the diffusivity of the matrix material is assumed to be $D = 1$.

If the inclusion has the same transport properties as those of the matrix phase, a uniform flow occurs with $q = 1$ at all points, according to theory. The numerical solution accurately represents the theoretical potential field, $u = x$, as indicated by the small relative error

$$e_r = \frac{\|u - u^h\|_2}{\|u\|_2} = 7.596 \times 10^{-8} \tag{9}$$

in terms of the L_2 error norm

$$\|u - u^h\|_2 = \sqrt{\sum_{I=1}^{N} (u(\mathbf{x}_I) - u^h(\mathbf{x}_I))^2} \tag{10}$$

where $u(\mathbf{x}_I)$ and $u^h(\mathbf{x}_I)$ are the exact solution and the numerical solution, respectively, at the location of node I; N is the total number of nodes. Over all nodes, the maximum local relative error is

$$\left\| \frac{u - u^h}{u} \right\|_\infty = 4.882 \times 10^{-7} \tag{11}$$

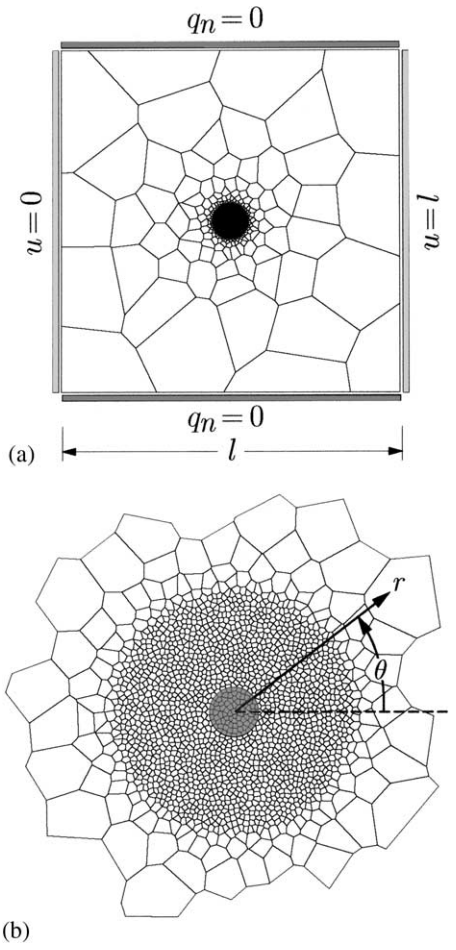

Fig. 4. (a) Computational mesh for steady-state flow analysis and (b) magnified region local to inclusion.

The network does not exhibit spurious heterogeneity arising from either random mesh geometry or varying element size.

The same problem is analyzed for an *impermeable* inclusion, as presented in Sukumar and Bolander [18]. Inclusion radius, a, is small relative to the domain size (i.e. $a = l/100$), so that comparisons can be made to the theoretical solution for an infinite domain:

$$\cos 2\theta = \frac{\left(\frac{a}{r}\right)^4 + 1 - q^2}{2\left(\frac{a}{r}\right)^2} \tag{12}$$

where (r, θ) forms the basis for a polar coordinate system, with its origin at the inclusion center (Fig. 4b), and q represents flow rate [19]. The accuracy of the model is demonstrated by comparing the numerical and theoretical flow values shown in Fig. 5. The contour lines produced from the numerical model (using the flux calculation method described in Section 3.1) follow the theoretical values and are smooth even in regions where the flow gradient is small. Significantly coarser discretizations provide fairly accurate results, although the flow rate curves are not as smooth and the curves closest to the inclusion are not captured.

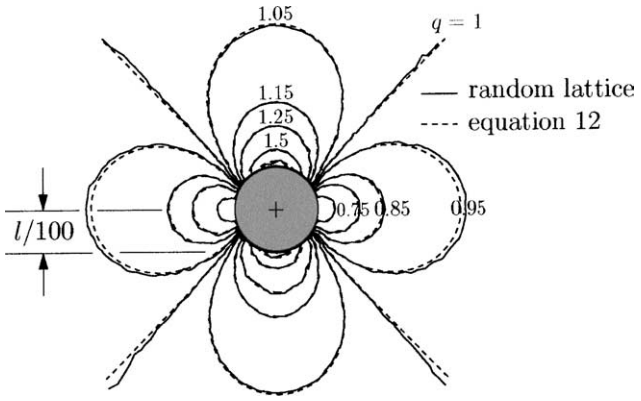

Fig. 5. Flow contours local to impermeable cylindrical inclusion.

3.3. Transient flow in a three-dimensional random lattice

Consider the initial value problem consisting of finding a function $u = u(t)$ satisfying the diffusion equation (Eq. (1)) and initial conditions $u(0)$. The semi-discrete form of Eq. (1) is

$$\mathbf{M}\dot{\mathbf{u}} + \mathbf{K}\mathbf{u} = \mathbf{f} \tag{13}$$

where the dot over $\mathbf{u}$ indicates time derivative [15]. The trapezoidal rule (Crank–Nicolson scheme) is used for stable solution of the linear diffusion equation, as outlined by Hughes [20].

As a benchmark problem for validating the material model and transient solution algorithm, a rectangular prism of length L (the symmetric portion of which is shown in Fig. 6) is given an initial potential distribution

$$u(x, y, z, t = 0) = \sin\left(\frac{\pi x}{L}\right) \tag{14}$$

where x is distance along the prism axis. Without loss of generality, the diffusivity coefficient, D, is assumed to be unity. The sides of the prism are assumed to be perfectly sealed, which renders this a one-dimensional flow problem. The solution is an exponential decay of the initial potential distribution

$$u(x, t) = \sin\left(\frac{\pi x}{L}\right) e^{\frac{-\pi^2 t}{L^2}} \tag{15}$$

A three-dimensional Voronoi diagram has been used to discretize the symmetric portion of the prism. The A_e term appearing in the element diffusivity matrix $\mathbf{K}_e$ (Eq. (6)) is the area of the Voronoi facet common to both nuclei of a given element. Fig. 6b shows, at each of several times during the solution history, there is no discernable difference between the nodal values from the three-dimensional numerical solution and the theoretical solution. Similar to the two-dimensional case, the model

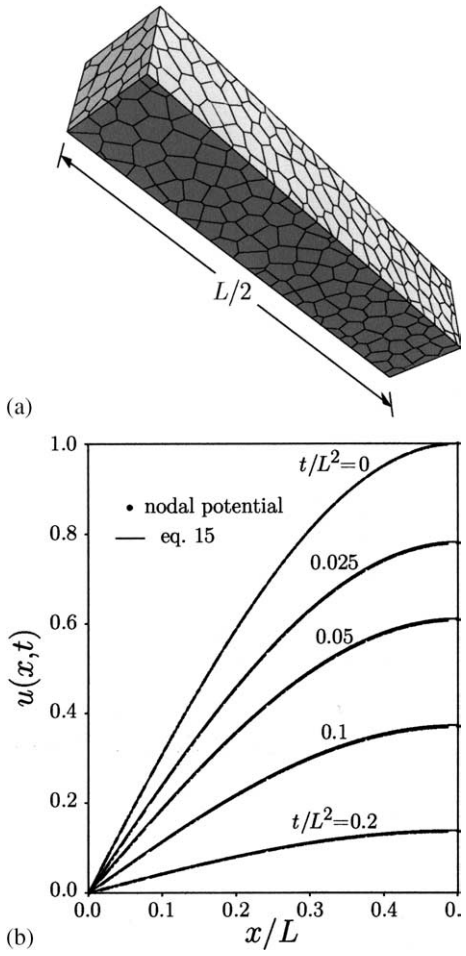

Fig. 6. Transient analysis of prism with prescribed initial potential distribution.

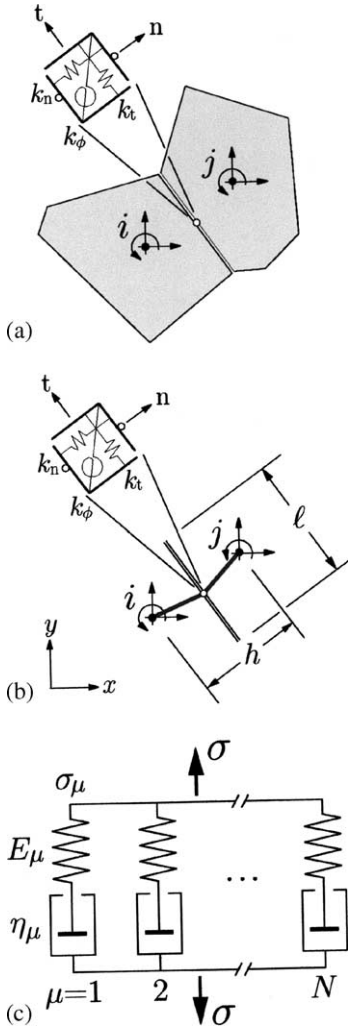

Fig. 7. RBSN basic element: (a) rigid cell depiction, (b) lattice element depiction, and (c) Maxwell chain model for representing material aging and basic creep processes.

exhibits no significant numerical noise due to random geometry of the network.

4. Rigid-body-spring networks

This section briefly summarizes previous development and application of rigid-body-spring networks (RBSN) to modeling the structural behavior of cement composites. In Section 5, the random lattice model of moisture transport is coupled with the RBSN to simulate drying shrinkage cracking.

4.1. Elasticity model

The RBSN approach has evolved from the rigid-body-spring concept of Kawai [12,21]. Basically, the material is discretized as a collection of rigid cells interconnected along their common boundaries by zero-size spring sets (Figs. 1 and 7). The cells are rigid only in the sense that they maintain their shape during material deformation; all flexibility is lumped into the intercell spring sets so that cell separation and overlapping generally occur.

The distinguishing features of the RBSN are [12,13]: (1) the cell geometries are defined by a Voronoi diagram, as described in Section 2, and (2) the cell degrees of freedom are defined at the corresponding cell nuclei. Each spring set consists of normal, tangential, and rotational springs that are assigned stiffnesses k_n, k_t, and k_ϕ, respectively. These stiffnesses are a simple function of the distance between the Voronoi cell nuclei, h, and the length of the common boundary segment, ℓ,

$$\begin{aligned} k_n &= Et_e\ell/h \\ k_t &= Et_e\ell/h \\ k_\phi &= k_n\ell^2/12 \end{aligned} \tag{16}$$

where E is the elastic modulus of the continuum material and t_e is the element thickness in a two-dimensional setting. The systematic scaling of the spring stiffnesses

given by Eq. (16) provide an elastically homogeneous representation of the continuum [12,13]. Note that the same A_e/h scaling relation is built into the diffusivity terms in Eq. (6), since $A_e = t_e\ell$ for the two-dimensional case.

From the arrangement of its six degrees of freedom, a two-cell subassembly is similar to a beam-spring element with axial stiffness. The RBSN is therefore akin to a random lattice network of beam elements, whose sectional properties are distributed according to the geometry of the Voronoi diagram. When modeling a multi-phase material, such as that shown in Fig. 1b, an individual element represents either one of the phases (which are often assumed to be homogeneous) or the interface between such phases. The ability to model homogeneous behavior is therefore of both fundamental and practical importance.

4.2. Basic creep model

To model basic creep processes active under sustained loading, σ, each lineal spring within the RBSN is replaced with a Maxwell chain model [22], as shown in Fig. 7c. These Maxwell chains represent the linear viscoelastic aging behavior of the cement-based material. The age dependent stiffnesses, $E_\mu(t)$, and viscosities, $\eta_\mu(t)$, of the Maxwell units correspond to terms in the Dirichlet series expansion of the material relaxation function [23]. Creep strains are determined for each time increment using an unconditionally stable algorithm, so that time step size can be increased as the creep rate decays.

For validating the above procedure, the simplified BP-KX model [24] is used to provide the compliance J for a typical concrete in a non-drying, constant temperature environment (from which the time-dependent moduli in Fig. 7c can be assigned). Fig. 8a shows both this compliance relation and the curve obtained from RBSN analysis of a homogeneous membrane structure under uniform compressive loading (Fig. 8b). A constant step size is used along the $\log(t - t')$ axis.

The RBSN model not only reproduces the global J curve, but also provides an accurate representation of local creep strains, as well as stresses, which are uniform over the network. Apart from elements aligned in the horizontal direction, all elements exhibit precisely the same creep as that measured globally. After a load duration of 1000 days, the vertical strains over each RBSN element, normalized by the global vertical strain, have a standard deviation of less than 1×10^{-4}.

4.3. Fracture model

Mode I cracking is simulated by degrading the strengths and stiffnesses of the intercell spring sets. The key feature of the RBSN fracture model is a crack band

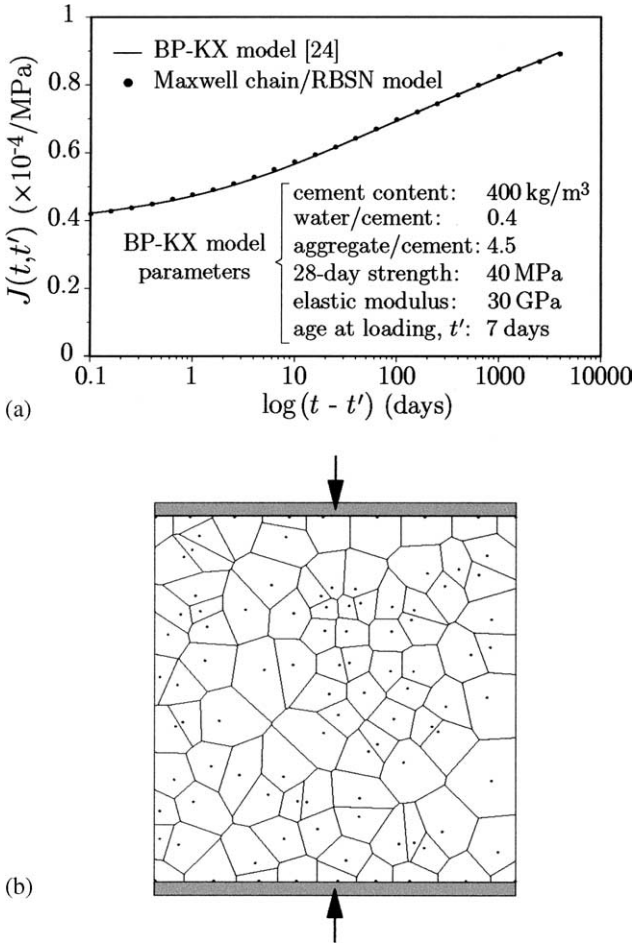

Fig. 8. Basic creep of a homogeneous membrane structure under compressive loading.

can form at an angle θ_R to the element axis and the dimensions of the crack band are determined accordingly (Fig. 9a) [13]. The forces carried by the spring sets are known at any stage of the loading history. An average value of tensile stress can be calculated from the resultant of this force pair, divided by the projected area

$$\sigma_R = \frac{F_R}{t\ell\cos\theta_R} \tag{17}$$

To obtain proper fracture energy consumption for different meshing strategies, strain values characterizing the softening response are dependent on crack band width, as described by Bažant and Oh [25].

$$\epsilon^{cr} = \frac{w}{h\cos\theta_R} \tag{18}$$

where w is the crack opening displacement. That is, mode I cracking is controlled by the shape of the tension softening diagram and the fracture energy, G_F, which is assumed to be a material property. The bi-linear softening diagram, shown in Fig. 9b, can be defined by stress and crack opening values determined through inverse analysis of fracture test results [13]. After each

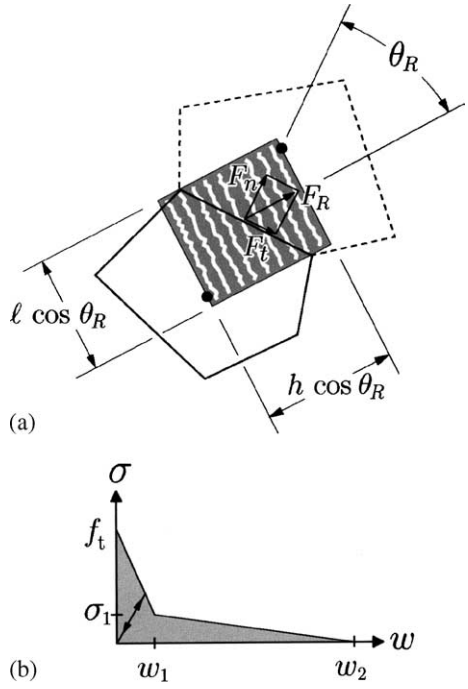

Fig. 9. Crack band formation within RBSN and associated softening relation.

load increment, the resultant tensile stress in each spring set is checked against the softening relation. For a critical spring set, fracture involves an isotropic reduction of the spring stiffnesses and an associated release of spring forces, so that the resultant stress lies on the corresponding softening relation. The release of spring forces causes an imbalance between the external and internal nodal force vectors, which is corrected through conventional equilibrium iterations. As for most lattice models, a maximum of one spring set is modified per iteration cycle. While this approach is computationally demanding, it is stable in that zero-energy modes of deformation are avoided.

The fracture model provides an objective representation of Mode I fracture, including fracture through random meshes [13]; uniform fracture energy is consumed along the crack length independent of mesh size and geometry. Practical application of the RBSN approach has been demonstrated through various analyses of structural concrete members [17].

5. Simulation of shrinkage cracking in overlay systems

The modeling of potential flow described in Section 3, coupled with the elasticity, creep, and fracture models described in Section 4, provide a basic framework for studying drying shrinkage cracking in cement composites. The following discussion of the nonlinear diffusion problem, the convective boundary conditions at the exposed surface, and the coupling of the stress and diffusion analyses, is based on work of Bažant and Najjar [26] and Martinola and Wittmann [1]. Since comparisons are made with third-party simulation results that did not include aging and creep effects, such phenomena are not included in the shrinkage crack simulations that follow. Tensile creep generally plays an important role in mitigating shrinkage crack development at early ages [27]. Other complicated behaviors associated with wetting and drying cycles [7], time-dependent crack growth [28,29], and the coupling of transport and damage [30–32] are also not included in this simulation, although such factors eventually need to be considered for modeling most practical durability concerns.

5.1. Background

For isothermal conditions, and no sinks (e.g. hydration) or sources present,

$$\frac{\partial H}{\partial t} = \mathrm{div}(D(H)\mathrm{grad}\ (H)) \tag{19}$$

where H is the pore relative humidity and $D(H)$ is the moisture dependent diffusion coefficient, which is a source of nonlinearity in the diffusion process [26]. Within the Crank–Nicolson solution scheme, iterations are performed to capture the nonlinear dependence of D on H to within a specified tolerance. The dependence of D on H can be approximated as:

$$D(H) = \beta e^{(\eta H)} \tag{20}$$

where β and η are fitted to experimental measurements [1]. When flux, q_s, occurs between the material boundary and the atmosphere, it is necessary to account for convective boundary condition

$$q_s = C_F(H_s - H_a) \tag{21}$$

where H_s and H_a are the relative humidities at the material boundary and in the surrounding atmosphere, respectively, and C_F is the film coefficient.

It is assumed that the diffusion process is uncoupled from the mechanical behavior of the material and any damage incurred during mechanical or hygral loading. This is a reasonable assumption for the microcracking that accompanies drying near the surface of the specimen [33], but needs further attention for more general situations. It is further assumed that the moisture distribution produces a shrinkage strain field according to

$$\Delta\epsilon_{sh} = \alpha_{sh}(H)\Delta H \tag{22}$$

where ϵ_{sh} is the shrinkage strain, ΔH is the moisture gradient and $\alpha_{sh}(H)$ is the hygral coefficient of shrinkage, which can be measured from drying tests at different relative humidities [1].

5.2. Model description

Consider the model shown in Fig. 10a, which represents a drying cement composite overlay on a mature concrete substrate. Symmetry conditions have been used so that only half the composite system is modeled. The top surface is exposed to the atmosphere with $H_a = 0.5$, while the other sides are assumed to be perfectly sealed.

This is the same problem studied numerically by Martinola and Wittmann [1] using the finite element method. This is the second case considered by those authors, where it is assumed that the substrate had not reached hygral equilibrium with the environment prior to application of the overlay. Rather, it has initial relative humidity $H = 0.9$ throughout its depth (except for a 20 mm layer at the top of the substrate which received moisture from the overlay process: it is assumed have initial $H = 1.0$).

The setup is treated as a three-phase system (i.e. overlay, substrate, and interface), with each phase having its own set of elasticity, hygral, and fracture parameters. For example, there are marked differences in the moisture diffusivity of the phases: the diffusivity of the overlay is the greatest at any given pore humidity, while that of the substrate is the least. Apart from one exception noted below, all input parameters and material relations are taken directly from the experimental measurements of Martinola and Wittmann [1], as presented in Table 1 where E is Young's modulus and f_t, σ_1, w_1, and w_2 correspond to the fracture softening parameters indicated in Fig. 9b. As shown in the table, two situations considered by Martinola and Wittmann are simulated here: (1) a weak, low G_F interface, and (2) a strong, tough interface. The film coefficient $C_F = 0.7$ mm/day. For direct comparisons with the results of Martinola and Wittmann, material aging and the creep model (and its mitigating effect on shrinkage stress development) have not been included in the simulation presented here.

5.3. Simulation results

To guage the accuracy of the lattice model and nonlinear solution procedure, the simulation results are compared with those from the commercial finite element package FEMLAB [35]. Fig. 11 shows relative humidity profiles for several times after the initiation of drying, along with the finite element mesh used for comparison. The same material parameters and boundary conditions have been used for each simulation. The terms in the diffusivity relations (Eq. (20)) were set to obtain humidity profiles similar to those obtained by Martinola and Wittmann [1].

Fig. 12a and b show contour maps of relative humidity and principal tensile stress, respectively, after 10 days exposure to the drying environment (with cracking suppressed in the lattice model). As is apparent from the stress contours, and has been noted elsewhere [1,5], there are two main potential fracture mechanisms: (1) tensile fracture of the overlay perpendicular to the interface, and (2) debonding of the overlay from the substrate due

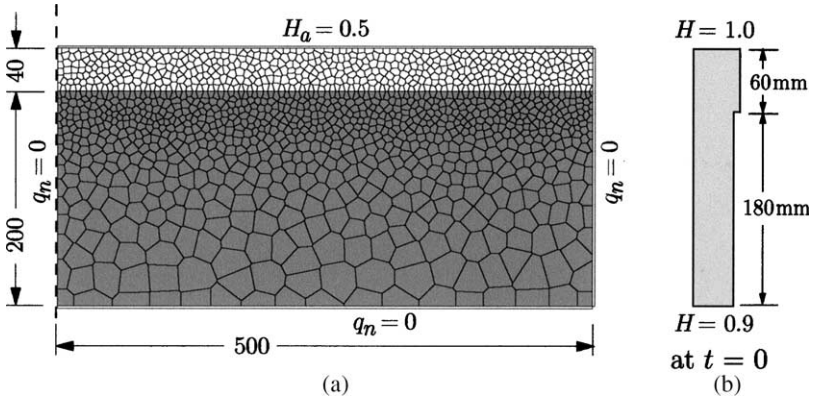

Fig. 10. Computational grid for the cement composite overlay system and initial moisture profile.

Table 1
Material properties used for analysis (from Martinola and Wittmann [1])

System component	α_{sh} 1/H	G_F N/m	E GPa	f_t MPa	σ_1 MPa	w_1 mm	w_2 mm
Overlay	0.0048	161	26.0	4.5	0.55	0.050	0.18
Interface (weak/brittle)	0.0028	32	28.0	1.0	0.33	0.024	0.12
Interface (strong/tough)	0.0028	129	28.0	4.0	0.50*	0.040*	0.20*
Substrate	0.0013	95	33.0	4.0	0.50	0.020	0.20

*Entries inferred from corresponding G_F value.

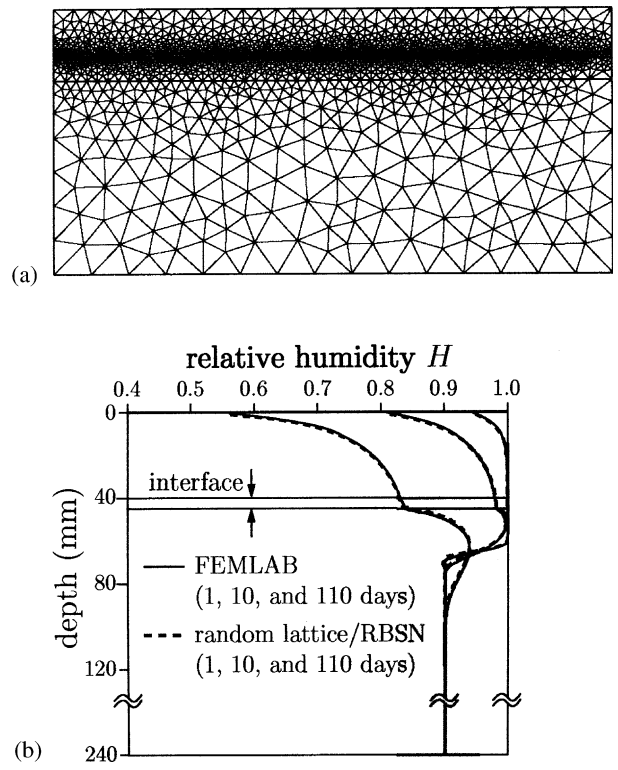

Fig. 11. (a) FEMLAB finite element mesh, and (b) computed moisture profiles across model mid-section.

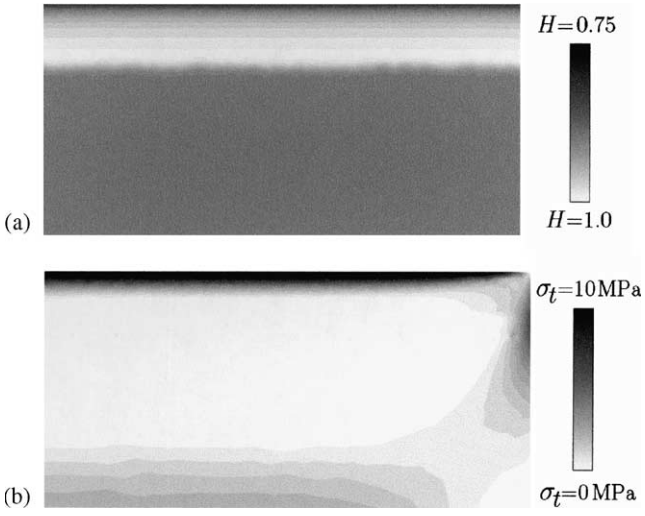

Fig. 12. Simulation results for 10 days exposure to drying environment: (a) relative humidity, and (b) principal tensile stress (with cracking suppressed).

to fracture along the interface, starting at the free end of the composite system.

For the weak interface specified in Table 1, debonding along the interface occurs prior to 20 days of drying and progresses from the end of the specimen as the overlay tends to warp (Fig. 13). When prescribing a strong interface, numerous fracture zones develop along the top of the overlay well before 20 days of drying.

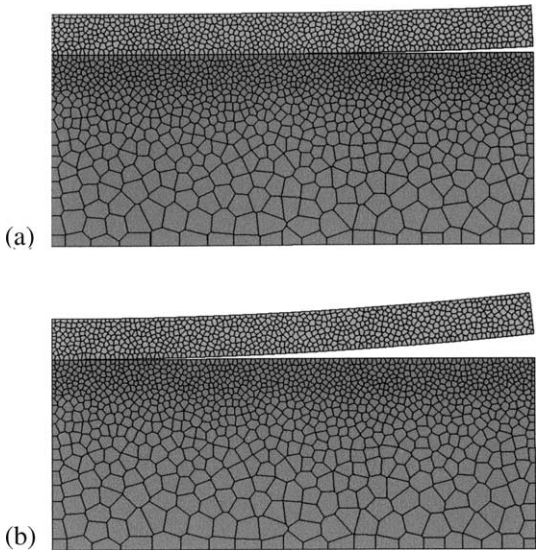

Fig. 13. Debonding along weak interface for: (a) 20 days and (b) 50 days exposure to drying environment.

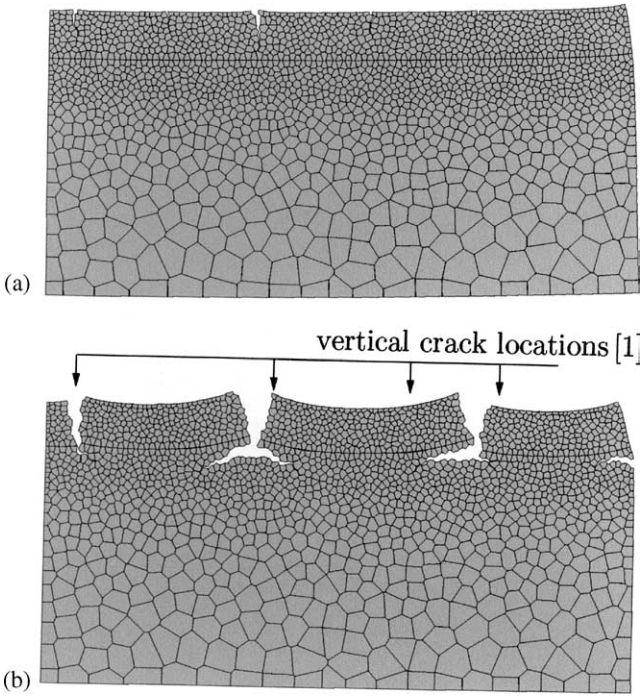

Fig. 14. Simulated deformation and crack patterns using a strong/tough interface: (a) 10 days and (b) 110 days exposure to drying environment.

Only a few of these fracture locations are discernable in Fig. 14a due to the scaling of the displacements. With shrinkage due to additional drying, localization occurs in that some of the cracks continue to open while neighboring cracks unload. Fig. 14b shows the specimen after 110 days of exposure to the drying environment. The cracking locations witnessed in the associated simulations of Martinola and Wittmann are also indicated in the figure. The pattern of cracks in the overlay, as well

as the tendency for overlay cracks to turn and run laterally, are in good general agreement with the results presented by Martinola and Wittmann. Such lateral branching of shrinkage cracks has also been witnessed by Bisschop [36].

6. Conclusion

Basic routines for the random lattice modeling of potential flow (e.g. moisture transport) in cement composites have been validated through benchmark comparisons with theory. When coupled with the RBSN, which accounts for the elastic, creep, and fracture properties of the material, the package provides a basic means for studying shrinkage crack development in the time domain. Simulations have been given, and compared to simulation results presented in the literature, for shrinkage cracking in a cement composite overlay on a mature concrete substrate. The results show the importance of the properties of the interfacial zone in determining the ultimate fracture mechanism: debonding of the overlay from the substrate or fracture through the thickness of the overlay.

The rather common approach for modeling transport and damage in concrete materials has been presented here, i.e. the concrete is regarded as a homogeneous medium and all the details of the transport and fracture processes have been lumped into the macroscopic diffusivity and fracture energy relations, respectively. Microstructural models are an alternative means to simulating material diffusivity [34]. One ultimate goal of this work is to connect the heterogeneous features present at finer scales of observation to behavior at the structural scale. The accurate simulation of potential flow about an impermeable inclusion was a step toward conducting such analyses. Clearly, inclusion type, volume fraction and distribution affect moisture transport, shrinkage, creep, and fracture, all of which strongly affect the durability of the system. However, the larger portion of the work presented here has been toward validating model abilities to represent fundamental aspects of moisture movement, shrinkage, and fracture within homogeneous systems. This is an essential starting point in the development of this lattice-type approach, prior to introducing heterogeneity and other complicating factors such as wetting and drying cycles, time-dependent crack growth, and the mutual coupling of transport and damage.

Acknowledgement

This work is currently supported by a US National Science Foundation grant (CMS-0201590) to the University of California at Davis.

References

[1] Martinola G, Wittmann FH. Application of fracture mechanics to optimize repair mortar systems. In: Wittmann FH, editor. Fracture Mechanics of Concrete Structures. Freiburg: AEDIFICATIO Publishers; 1995. p. 1481–6.
[2] Martinola G, Sadouki H, Wittmann FH. Numerical model for minimizing risk of damage in repair system. ASCE J Mater Civil Engng 2001;13(2):1481–6.
[3] Shah SP, Swartz SE, Ouyang C-S. Fracture mechanics of concrete—applications of fracture mechanics to concrete, rock, and other quasi-brittle materials. New York: John Wiley & Sons; 1995.
[4] Bažant ZP, Planas J. Fracture and size effect in concrete and other quasi-brittle materials. Boca Raton, Florida: CRC Press; 1998.
[5] Lange DA, Shin H-C. A computer-based design tool for analysis of bonded concrete overlays. Concrete Sci Engng 2001;3:189–94.
[6] Ulm F-J, Rossi P, Schaller I, Chauvel D. Durability scaling of cracking in HPC structures subject to hygromechanical gradients. ASCE J Struct Engng 1999;125(6):693–702.
[7] Maekawa K, Chaube R, Kishi T. Modeling of concrete performance—hydration, microstructure formation and mass transport. London: E&FN Spon; 1999.
[8] Herrmann HJ, Roux S, editors. Statistical models for the fracture of disordered media. Amsterdam: Elsevier/North Holland; 1990. 353 pp.
[9] Schlangen E, van Mier JGM. Experimental and numerical analysis of micromechanisms of fracture of cement-based composites. Cement Concrete Compos 1992;14:105–18.
[10] Sadouki H, van Mier JGM. Analysis of hygral induced crack growth in multiphase materials. HERON 1996;41(4):267–86.
[11] van Mier JGM, Vervuurt A, van Vliet MRA. Materials engineering of cement-based composites using lattice type models. In: Carpinteri A, Aliabadi MH, editors. Computational Fracture Mechanics in Concrete Technology. Southampton, UK: WIT Press; 1999. p. 1–32.
[12] Bolander JE, Saito S. Fracture analysis using spring networks with random geometry. Engng Fract Mech 1998;61:569–91.
[13] Bolander JE, Moriizumi K, Kunieda M, Yip M. Rigid-body-spring network modeling of cement based composites. In: de Borst R, Mazars J, Pijaudier-Cabot G, van Mier JGM, editors. Fracture Mechanics of Concrete Structures. Lisse, The Netherlands: AA Balkema Publishers; 2001. p. 773–80.
[14] Okabe A, Boots B, Sugihara K. Spatial tessellations—concepts and applications of Voronoi diagrams. Chichester, UK: John Wiley & Sons; 1992.
[15] Lewis RW, Morgan K, Thomas HR, Seetharamu KN. The finite element method in heat transfer analysis. Chichester, UK: John Wiley & Sons; 1996.
[16] Sukumar N. Voronoi cell finite difference method for the diffusion operator on arbitrary unstructured grids. Int J Numer Meth Engng 2003;57(1):1–34.
[17] Bolander JE, Hong GS. Rigid-body-spring network modeling of prestressed concrete members. ACI Struct J 2002;99(5):595–604.
[18] Sukumar N, Bolander JE. Numerical computation of discrete differential operators on non-uniform grids. Computer Model Engng Sci, submitted for publication.
[19] Kirchhoff RH. Potential flows: Computer graphic solutions. New York: Dekker; 1985.
[20] Hughes TJR. Finite element method—linear static and dynamic finite element analysis. Englewood Cliffs, New Jersey: Prentice-Hall; 1987.
[21] Kawai T. New discrete models and their application to seismic response analysis of structures. Nucl Engng Des 1978;48:207–29.
[22] Bolander JE, Berton S, Emerick E. Inclusion interaction effects on concrete creep. In: Ulm F-J, Bažant ZP, Wittmann FH, editors.

6th international conference on creep, shrinkage and durability mechanics of concrete and other quasi-brittle materials (Concreep 6). Oxford, UK: Elsevier Science Ltd, 2001. p. 89–94.
[23] Bažant ZP. Material models for structural analysis. In: Bažant ZP, editor. Preprints of fourth RILEM international symposium on creep and shrinkage of concrete: mathematical modeling. RILEM, 1986. p. 80–232.
[24] Bažant ZP, Panula L, Kim J-K, Xi Y. Improved prediction model for time-dependent deformations of concrete: Part 6—Simplified code-type formulation. Mater Struct 1992;25:219–23.
[25] Bažant ZP, Oh BH. Crack band theory for fracture of concrete. Mater Struct 1983;16:155–76.
[26] Bažant ZP, Najjar LJ. Drying of concrete as a nonlinear diffusion problem. Cement Concrete Res 1971;1:461–73.
[27] Altoubat SA, Lange DA. Creep, shrinkage, and cracking of restrained concrete at early age. ACI Mater J 2001;98(4):323–31.
[28] Bažant ZP, Gettu R. Rate effects and load relaxation in static fracture of concrete. ACI Mater J 1992;89(5):456–68.
[29] Bažant ZP, Xiang Y. Crack growth and lifetime of concrete under long time loading. J Engng Mech 1997;123(4):350–8.
[30] Wang K, Jansen DC, Shah SP, Karr AF. Permeability study of cracked concrete. Cem Conc Research 1997;27(3):381–93.
[31] Gérard B, Marchand J. Influence of cracking on the diffusion properties of cement-based materials, Part I: Influence of continuous cracks on the steady-state regime. Cement Concrete Res 2000;30:37–43.
[32] Ababneh A, Xi Y, Willam, K. Multiscale modeling of the coupled moisture diffusion and drying shrinkage of concrete. In: Ulm F-J, Bažant ZP, Wittmann FH, editors. 6th International Conference on Creep, Shrinkage and Durability Mechanics of Concrete and Other Quasi-Brittle Materials (Concreep 6). Oxford, UK: Elsevier Science Ltd, 2001. p. 159–64.
[33] Wittmann FH. Influence of drying induced damage on the hygral diffusion coefficient. In: Wittmann FH, editor. Fracture Mechanics of Concrete Structures. Freiburg: AEDIFICATIO Publishers; 1995. p. 1519–25.
[34] Marchand J, Gérard B. New developments in the modeling of mass transport processes in cement-based composites—a review. In: Advances in concrete technology-Proceedings Second International CANMET/ACI International Symposium (SP-154). Farmington Hills, Michigan: American Concrete Institute, 1995. p. 169–210.
[35] FEMLAB v2.3, COMSOL AB, Stockholm, Sweden, 2002.
[36] Bisschop J. Drying shrinkage microcracking in cement-based materials. PhD Thesis, Delft University of Technology, Delft, 2002.